Materials Research Express

PAPER

Effects of Er^{3+} concentration on the structure and optical properties of the $MgAl_2O_4/MgO/Sr_3Al_2O_6/SrAl_2O_4$ mixed phases prepared by the citrate sol gel method

C Dlamini[1,*], M R Mhlongo[1], L F Koao[2], T E Motaung[3], T T Hlatshwayo[4], Y Dwivedi[5] and S V Motloung[1,6,*]

[1] Department of Physics, Sefako Makgatho Health Science University, P. O. Box 94, Medunsa, 0204, South Africa
[2] Department of Physics, University of the Free State (Qwaqwa Campus), Private Bag X 13, Phuthaditjhaba, 9866, South Africa
[3] Department of Chemistry, University of Zululand, KwaDlangezwa, 3886, South Africa
[4] Department of Physics, University of Pretoria, Pretoria, 0002, South Africa
[5] Department of Physics, National Institute of Technology Kurukshetra, Haryana 136119, India
[6] Department of Physics, Nelson Mandela University, P. O. Box 77000, Port Elizabeth 6031, South Africa
[*] Authors to whom any correspondence should be addressed.

E-mail: dlaminiclinton@gmail.com **and** cchataa@gmail.com

Keywords: $MgAl_2O_4$, $Sr_3Al_2O_6$, $SrAl_2O_4$, Er^{3+}-doped, MgO, Sol-gel

OPEN ACCESS

RECEIVED
16 August 2020

REVISED
22 September 2020

ACCEPTED FOR PUBLICATION
30 September 2020

PUBLISHED
9 October 2020

Abstract

The mixed phases of the un-doped $MgAl_2O_4/MgO/Sr_3Al_2O_6/SrAl_2O_4$ (MMSS), $MgAl_2O_4/MgO$ (MM) $Sr_3Al_2O_6/SrAl_2O_4$ (SS), and the doped MMSS:x% Er^{3+} ($0 \leqslant x \leqslant 1.8$) nanopowders were synthesized using the citrate sol-gel method. The effect of Er^{3+} concentration on the structure, morphology and optical properties were investigated. X-ray powder diffraction (XRD) analysis indicated the cubical $MgAl_2O_4$, MgO and $Sr_3Al_2O_6$; and monoclinic $SrAl_2O_4$ phases. The scanning electron microscopic images revealed the transformation of irregular particles to rod-like structure with an increase in Er^{3+} concentration. Transmission electron microscope indicated the nanosized particles depends on Er^{3+} concentration. Severals distinct absorption bands located at 444, 546, 653 and 704 nm under UV excitation (285 nm) corresponding to the defects states of the $MgAl_2O_4$, MgO, $SrAl_2O_4$, and $Sr_3Al_2O_6$ phases were observed. There were traces of emission peaks at 546 and 653 nm attributed to the $^4S_{3/2} \rightarrow {}^4I_{15/2}$ and $^4F_{9/2} \rightarrow {}^4I_{15/2}$ transitions of Er^{3+} ion. An exponential decrease in luminescence was observed with an increase in Er^{3+} concentration.

1. Introduction

The advancement of new luminescent materials has attracted many researchers due to their compelling properties as a function of crystalline size and technological applications [1]. Among many studied luminescent materials, magnesium aluminate ($MgAl_2O_4$), magnesium oxide (MgO) and strontium aluminates ($Sr_3Al_2O_6$ and $SrAl_2O_4$) have shown great interest to many researchers due to their fascinating properties [2–4]. $MgAl_2O_4$ is described as an AB_2O_4 spinel and exhibits a cubic structure consisting of face centred cubic (fcc) structure [5]. The $MgAl_2O_4$ has a wide band gap ~5.82 eV [6]. MgO with band gap of ~5.26 eV [7] has been reported to be a promising inorganic material which can show crystallization in sodium chloride structure [7]. It has many applications such as in optical coatings, sensor, water treatment, catalysis and antimicrobial [8]. $Sr_3Al_2O_6$ is another interesting compound which was used to make transparent ceramics, mechanoluminescence, long lasting luminescence etc [9]. Mindru *et al* [10] reported cubical symmetry of $Sr_3Al_2O_6$ phase having wide band gap ~6.3 eV [11]. $SrAl_2O_4$ is considered a good luminescent material and a higher chemical stability with wide band gap ~6.5 eV [12]. Garcia *et al* [13] reported that $SrAl_2O_4$ consist of monoclinic phase structure. Different methods have been used to synthesize the bulk materials of the $MgAl_2O_4$, MgO, $Sr_3Al_2O_6$ and $SrAl_2O_4$ such as hydrothermal synthesis [14], solid-state reaction [15], precipitation [16], combustion method [17] and citrate sol-gel method [18]. The citrate sol-gel method was used in this study as it is economical, low temperatures ~80 °C synthesis, less time consuming, and having good control of morphological particles. These wide band

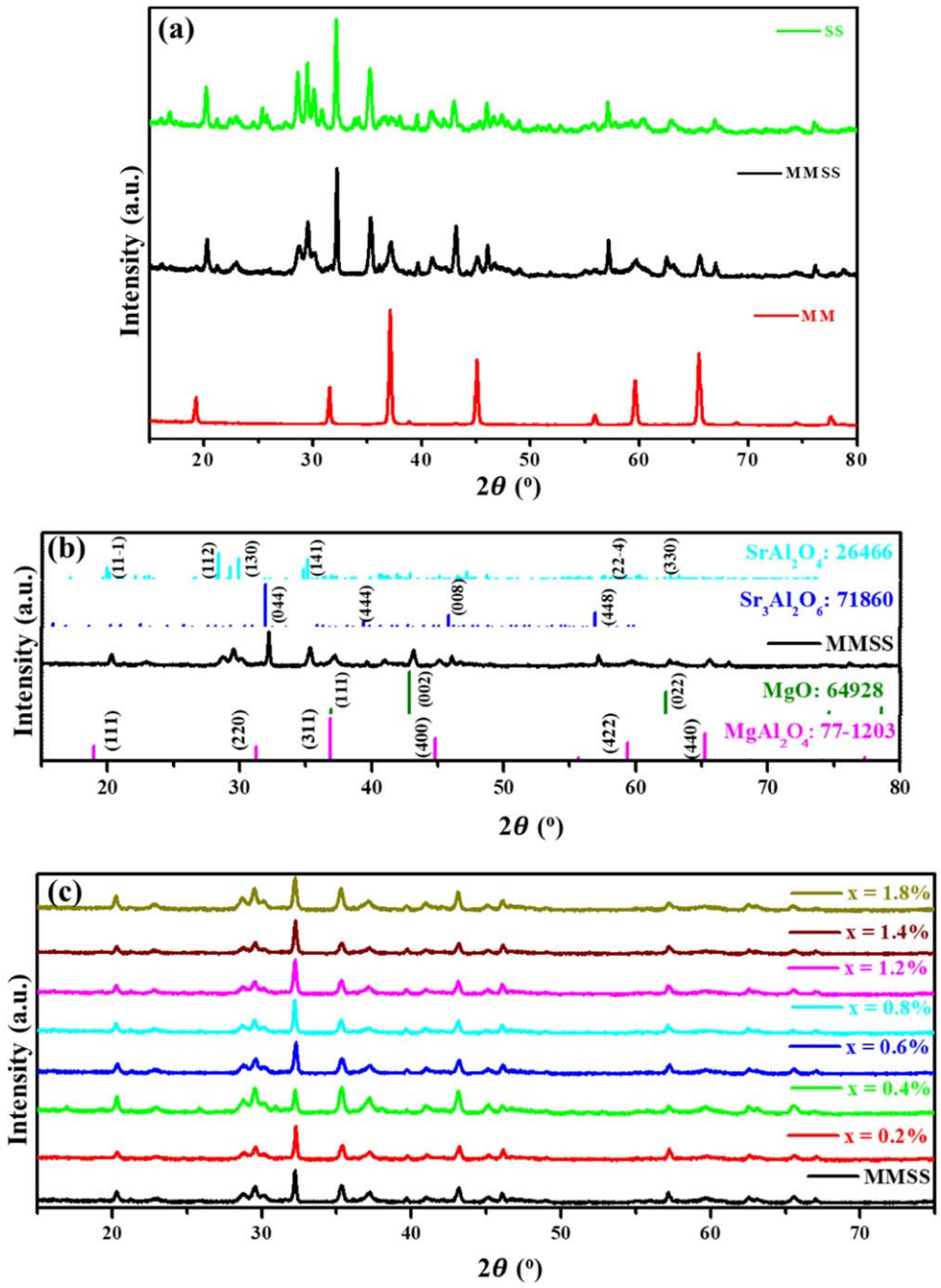

Figure 1. XRD patterns of the (a) un-doped MMSS, MM, SS phases (b) un-doped MMSS, ICSD files of $MgAl_2O_4$, MgO, $Sr_3Al_2O_4$, $SrAl_2O_4$ and (c) MMSS:x% Er^{3+} ($0 \leqslant x \leqslant 1.8$) samples.

gap materials can be made to emit emission in visible- infrared (IR) region by activating the host matrix by foreign atoms such as the lanthanide rare earth (Ln) metals [19]. One good example of the Ln is Er^{3+} ion. Er^{3+} is one of efficient ions to achieve IR to visible up-conversion [20]. Mironova-Ulmane *et al* [21] reported a study on the up and down conversion analysis of Er^{3+} doped on $MgAl_2O_4$ spinel matrix. The emission results showed peaks at 550 and 660 nm, which were attributed to the $^4S_{3/2} \rightarrow {}^4I_{15/2}$ and $^4F_{9/2} \rightarrow {}^4I_{15/2}$ transitions of Er^{3+}. Balakrishnan *et al* [8] reported the study of optical and photocatalytic properties of MgO nanoparticles via combustion method. The PL results showed that under excitation of 385 nm three emissions were observed at 425, 461, and 495 nm which were attributed to defects band transition and oxygen vacancies. Choudhary *et al* [22] reported a study on effect of the Er^{3+}, Yb^{3+} and Zn^{2+} ion concentration and temperature on the up-conversion behaviour of Er^{3+}/Yb^{3+} co-doped $SrAl_2O_4$ phosphor. The study of Er^{3+} and Er^{3+}/Yb^{3+} co-doped $Sr_3Al_2O_6$ phosphors was carried out by Singh *et al* [23], in which sample was prepared via a soft combustion synthesis route. The UV-Visible absorption results suggested that the presence of various bands correspond to the doped trivalent Ln ions. With this previous reports, it is clear that the investigations of doping the Er^{3+} on the single phases or bulk materials ($MgAl_2O_4$, MgO, $Sr_3Al_2O_6$ and $SrAl_2O_4$) and other related foreign ions have

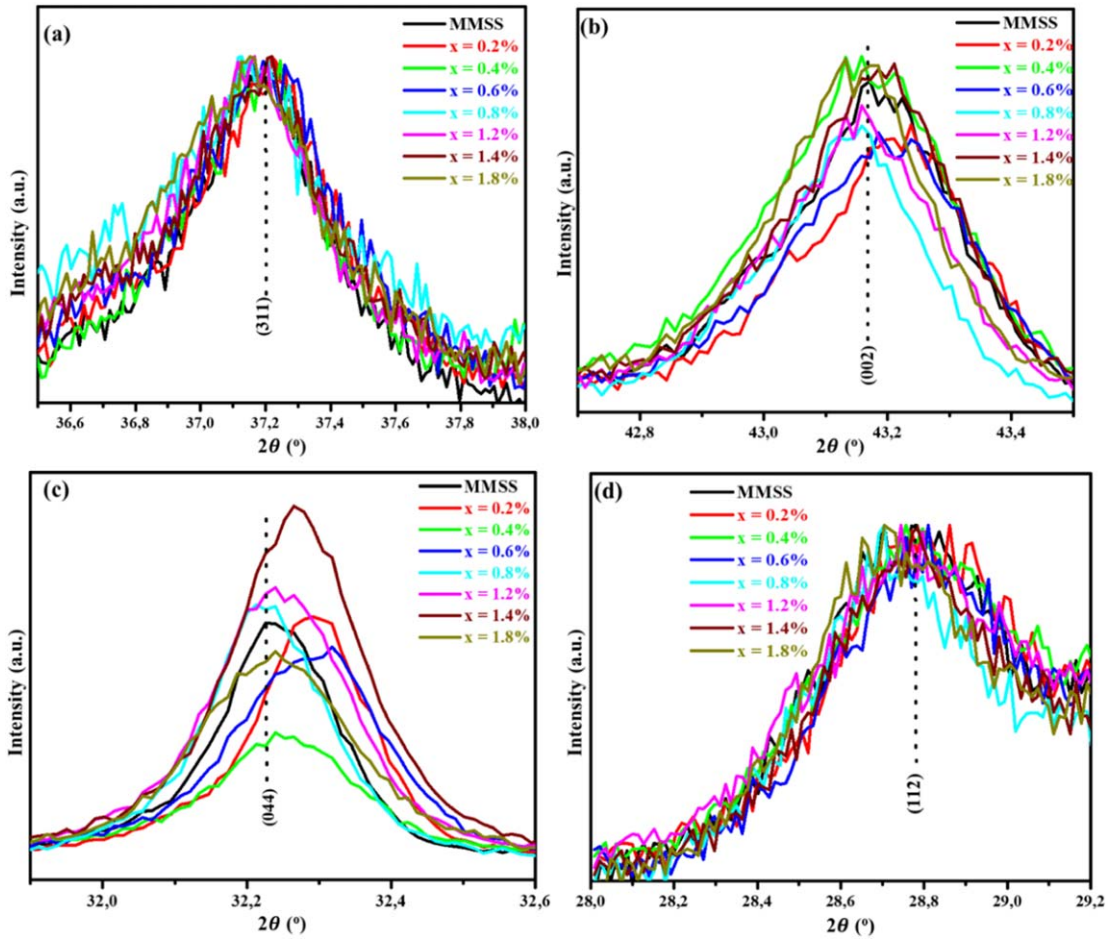

Figure 2. The analysis of the (a) crystalographic plane (311) of $MgAl_2O_4$; (b) plane (002) MgO, (c) plane (044) $Sr_3Al_2O_6$ and (d) plane (112) of $SrAl_2O_4$ for the MMSS:x% Er^{3+} ($0 \leqslant x \leqslant 1.8$) samples.

Table 1. Phase quantification of $MgAl_2O_4$, MgO, $Sr_3Al_2O_6$ and $SrAl_2O_4$.

Sample ID	$MgAl_2O_4$ (%)	MgO (%)	$Sr_3Al_2O_6$ (%)	$SrAl_2O_4$ (%)
MMSS	24.8	16.8	14.3	44.0
x = 0.2%	23.0	19.3	18.4	39.3
x = 0.4%	27.3	17.1	8.10	47.4
x = 0.6%	20.4	18.0	18.4	43.3
x = 0.8%	11.8	19.6	21.2	47.4
x = 1.2%	20.2	17.9	22.4	39.6
x = 1.4%	17.4	17.9	24.6	40.0
x = 1.8%	16.8	18.4	15.0	49.8

already been reported in literature [21–23]. However, there is no evidence on the studies of the mixed phases of $MgAl_2O_4/MgO/Sr_3Al_2O_6/SrAl_2O_4$ doped with Er^{3+} which have been reported to date. Thus, this study is aimed at investigating the effects of Er^{3+} concentration on the structure, morphology and optical properties of $MgAl_2O_4/MgO/Sr_3Al_2O_6/SrAl_2O_4$ prepared by citrate sol gel method. The main objective is to fabricate better luminescent materials for practical applications such as the light emitting diode (LED). Emission channels associated with the observed emissions are also proposed.

2. Experimental

2.1. Synthesis

The citrate sol-gel method was opted for the synthesis of various samples i.e. un-doped MMSS, MM ($MgAl_2O_4$ and MgO), SS ($SrAl_2O_4$ and $Sr_3Al_2O_6$) and MMSS:x% Er^{3+} ($0 \leqslant x \leqslant 1.8$). All of the chemicals used in this study

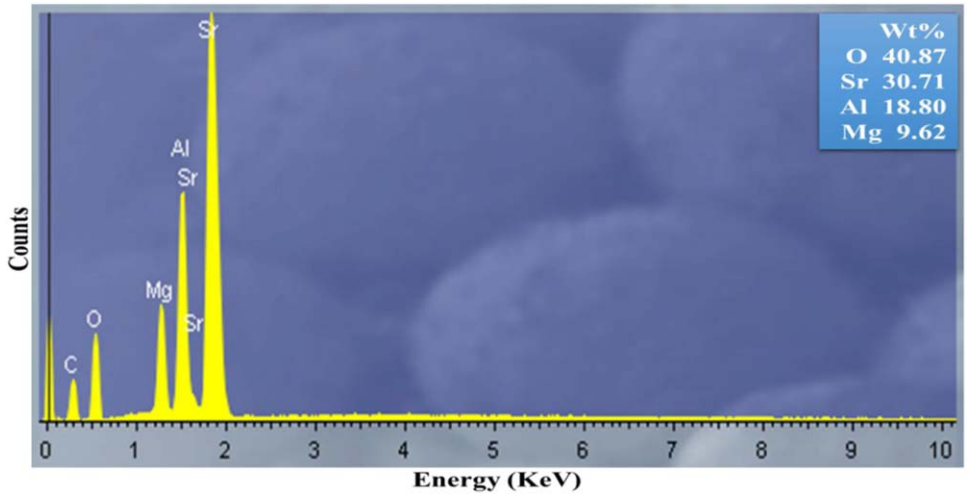

Figure 3. EDS spectrum of the un-doped MMSS.

Table 2. Summary of the crystallite size estimated by considering planes of different phases.

	Crystal size (nm)			
Sample ID	$MgAl_2O_4$ (311)	MgO (002)	$Sr_3Al_2O_6$ (044)	$SrAl_2O_4$ (112)
MMSS	23	40	60	17
x = 0.2%	22	38	59	18
x = 0.4%	24	37	51	15
x = 0.6%	21	37	46	17
x = 0.8%	19	41	56	17
x = 1.2%	21	38	49	15
x = 1.4%	21	40	51	18
x = 1.8%	19	43	45	17

were purchased at Sigma Aldrich. The un-doped MMSS sample was prepared by mixing appropriate amount of 3.808 g $Mg(NO_3)_2.6H_2O$ (98%), 3.411 g $Sr(NO_3)_2.4H_2O$ (99%), 10.919 g $Al(NO_3)_3.9H_2O$ (98%) and 2.328 g citric acid $C_8H_8O_7.H_2O$ (99%), respectively in 30 ml deionized water. Similarly, for un-doped MM ($MgAl_2O_4$/MgO) and SS ($SrAl_2O_4$ and $Sr_3Al_2O_6$) samples separate bulk solutions were prepared by dissolving same desired amount of $Mg(NO_3)_2.6H_2O$ (98%), $Al(NO_3)_3.9H_2O$ (98%) and $Sr(NO_3)_2.4H_2O$ (99%) in separate 30 ml deionized water, in which citric acid was added later on. The doped samples were prepared by adding the required amount of $ErCl_3.6H_2O$ (99.99%) for a range ($0 \leqslant x \leqslant 1.8$) in an un-doped MMSS solution. A magnetic stirrer was used to constantly stir the different solutions which was kept at ~80 °C temperature until transparent solution gels were formed. Initially, the gels were dried in an oven for an hour at 130 °C and later on annealed at 1200 °C for 2 h until white powders were formed. The powders were taken for characterizations using different techniques.

2.2. Characterization

The XRD Bruker D8-Adance powder diffractometer with a Cu-K_α (1.5405 Å) radiation was used to characterize the crystal structure of the prepared nanopowders. The phases were identified using X'Pert Highscore plus software. The relative phase amounts (weight %) were estimated using the Rietveld method. The Zeiss Supra-55 scanning electron microscope (SEM) coupled with an energy dispersive x-ray spectroscopy (EDS) was used to analyse the surface morphology and elementary composition of the prepared nanopowders. JEOL JEM 1010 transmission electron microscopy (TEM) was used to study the particle size of the prepared nanopowder samples. The absorption characteristics of the prepared samples were investigated on the Perkin-Elmer LS-55 UV–vis spectrophotometer. The Hitachi F-7000 fluorescence spectrophotometer was used to monitor photoluminescence spectra and radiative decay curves.

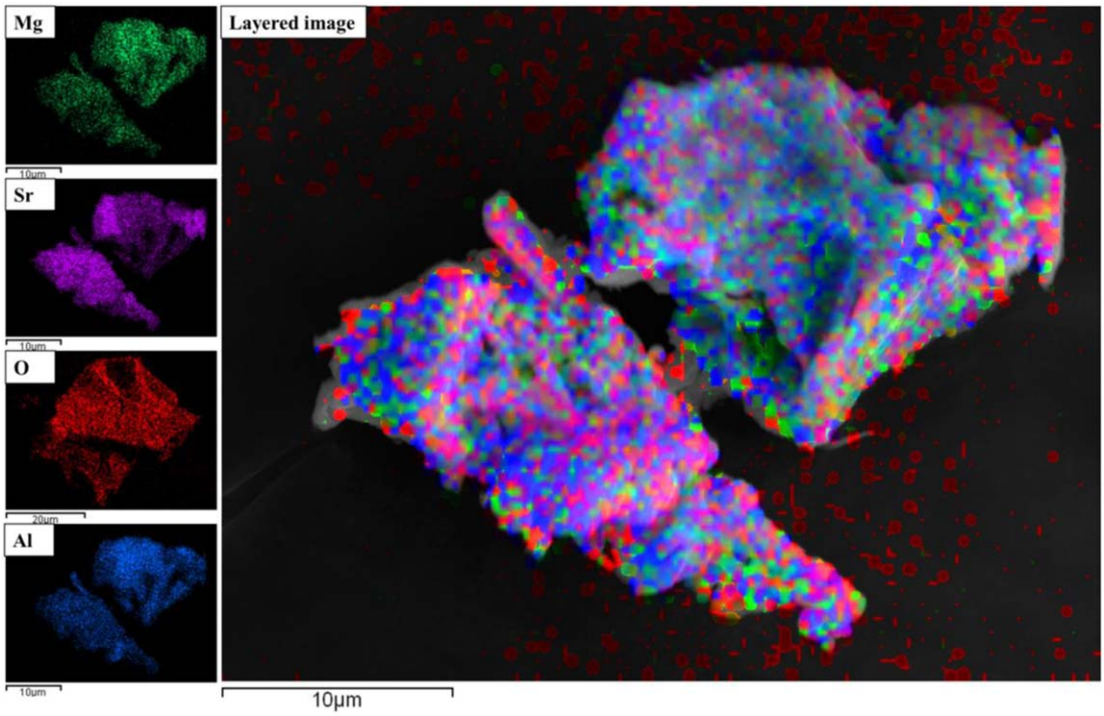

Figure 4. EDS elemental map of the un-doped MMSS sample.

3. Results and discussion

3.1. XRD analysis

Figure 1(a) shows the x-ray patterns of the un-doped MMSS, MM and SS phases which correspond to the diffraction patterns of cubic $MgAl_2O_4$ and MgO samples matches well with the standard ICSD no. 77-1203 and 64 928, respectively shown in figure 1(b). On the other hand strontium aluminate sample exhibits two phases namely cubical $Sr_3Al_2O_6$; (ICSD: 71860) and monoclinic $SrAl_2O_4$ (ICSD: 26466) phases. Furthermore, magnesium strontium aluminate sample co-exhibits four crystallographic phases of the MMSS. The quantification of each phase present in MMSS is presented in table 1. Figure 1(c) shows the patterns of the MMSS:x% Er^{3+} ($0 \leqslant x \leqslant 1.8$) samples, which revealed similar patterns as obtained in the un-doped MMSS sample shown in figure 1(a). This observation reveal that Er^{3+} ion doping did not affect the crystal structure of the phases within MMSS.

The analysis of the most intense peaks (311), (002), (044) and (112) of the $MgAl_2O_4$, MgO, $Sr_3Al_2O_6$ and $SrAl_2O_4$ phases are shown in figure 2, respectively. Figure 2(a) shows the most intense diffraction peak (311) of $MgAl_2O_4$ phase does not have significant peak shift with the Er^{3+} ion doping. This is attributed to the comparison of the ionic radius of Mg^{2+} (0.72 Å) [5], which is comparable to the Er^{3+} ionic size (0.88 Å) [24] and hence possibility of Mg ion substitution cannot be ruled out. Similar results were observed in our previous study of $MgAl_2O_4$:Mn^{2+} Dlamini *et al* [25]. Figure 2(b) shows the most intense peak (002) of MgO phase which generally indicates that at $\leqslant$0.6% Er^{3+} the peaks slightly shifted to higher angle while at the $\geqslant$0.8% Er^{3+} the diffraction peak was slightly shifted to lower angle. The results therefore revealed that the lattice constant in the case of MgO depends on the Er^{3+} concentration. In the plane (044) corresponding to the $Sr_3Al_2O_6$ phase shown in figure 2(c), the results generally show that for the $\leqslant$0.6% Er^{3+} the diffraction peak (in comparison to the MMSS) shifted towards higher angles, while there was no shift for the $\geqslant$0.8% Er^{3+}. Comparing the ionic radius of Er^{3+} (0.88 Å) with Sr^{2+} (1.21 Å) [26] and Al^{3+} (0.53 Å), the difference between the ionic radius is similar i.e. 0.33 Å and 0.35 Å for for Sr^{2+} and Al^{3+} with Er^{3+} ion, it becomes a difficult task for the substitution of Er^{3+} either to Al^{3+} or Sr^{2+}. Further, it is obvious that to accommodate Er^{3+} ion at Sr^{2+} site, charge compensation is required although at Al^{3+} ion site charge compensation is not required. Apparently Er^{3+} ion may substitute Al^{3+} ion in $Sr_3Al_2O_6$ and $SrAl_2O_4$ phases. It is expected that due to the higher coordination number of Al^{3+} ion site in $Sr_3Al_2O_6$ phase, Er^{3+} ion would prefer to accommodate in (cubical) $Sr_3Al_2O_6$ phase rather in distorted (monoclinic) $SrAl_2O_4$ phase [27]. In the case of plane (112) of $SrAl_2O_4$ phase shown in figure 2(d), the peak slightly shifted to lower angles. This is attributed to similar observation and explanation in figure 2(b).

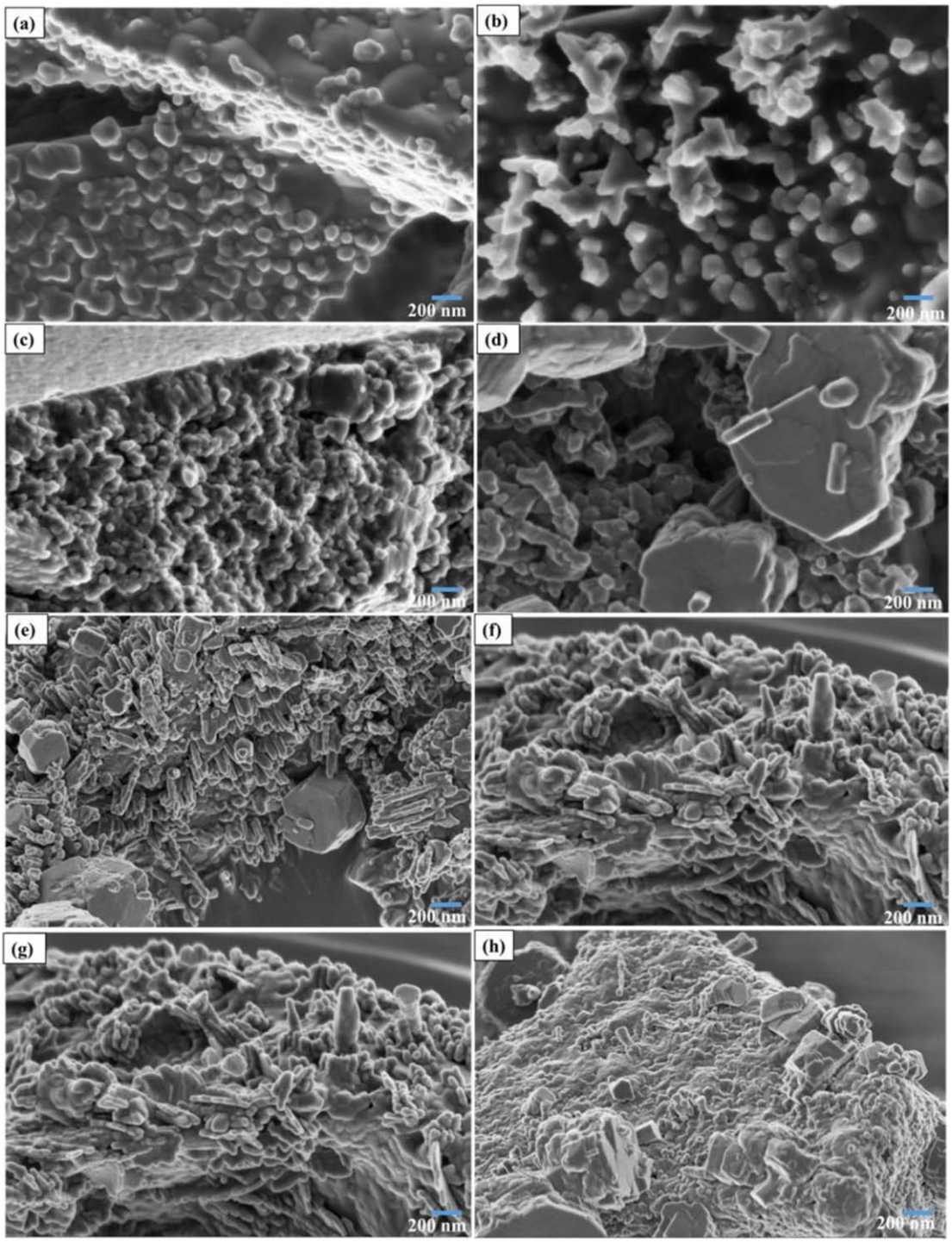

Figure 5. SEM images of the (a) un-doped MMSS, (b) x = 0.2% (c) 0.4% (d) 0.6% (e) 0.8% (f) 1.2% (g) 1.4% and (h) 1.8% Er^{3+}.

The crystallite sizes of the MMSS mixed phases shown in table 2 were estimated using the Scherrer's equation (1) [28]. The crystal sizes were estimated from the most intense diffraction peaks (311), (002) (044) and (112) of the $MgAl_2O_4$, MgO, $Sr_3Al_2O_6$ and $SrAl_2O_4$ phases, respectively. It can be observed from table 2 that varying the Er^{3+} concentration slightly affected the size of crystallite size. Overall, the crystalline size reduces in doped than the un-doped sample. However, the crystalline size corresponding to $SrAl_2O_4$ phase is smaller than other phases.

3.2. EDS analysis

The EDS spectrum of the un-doped MMSS sample is shown in figure 3. The spectrum confirms the presence of the Mg, Sr, Al and O elements in the prepared samples. The observed extra peak of carbon (C) around 0.3 eV is

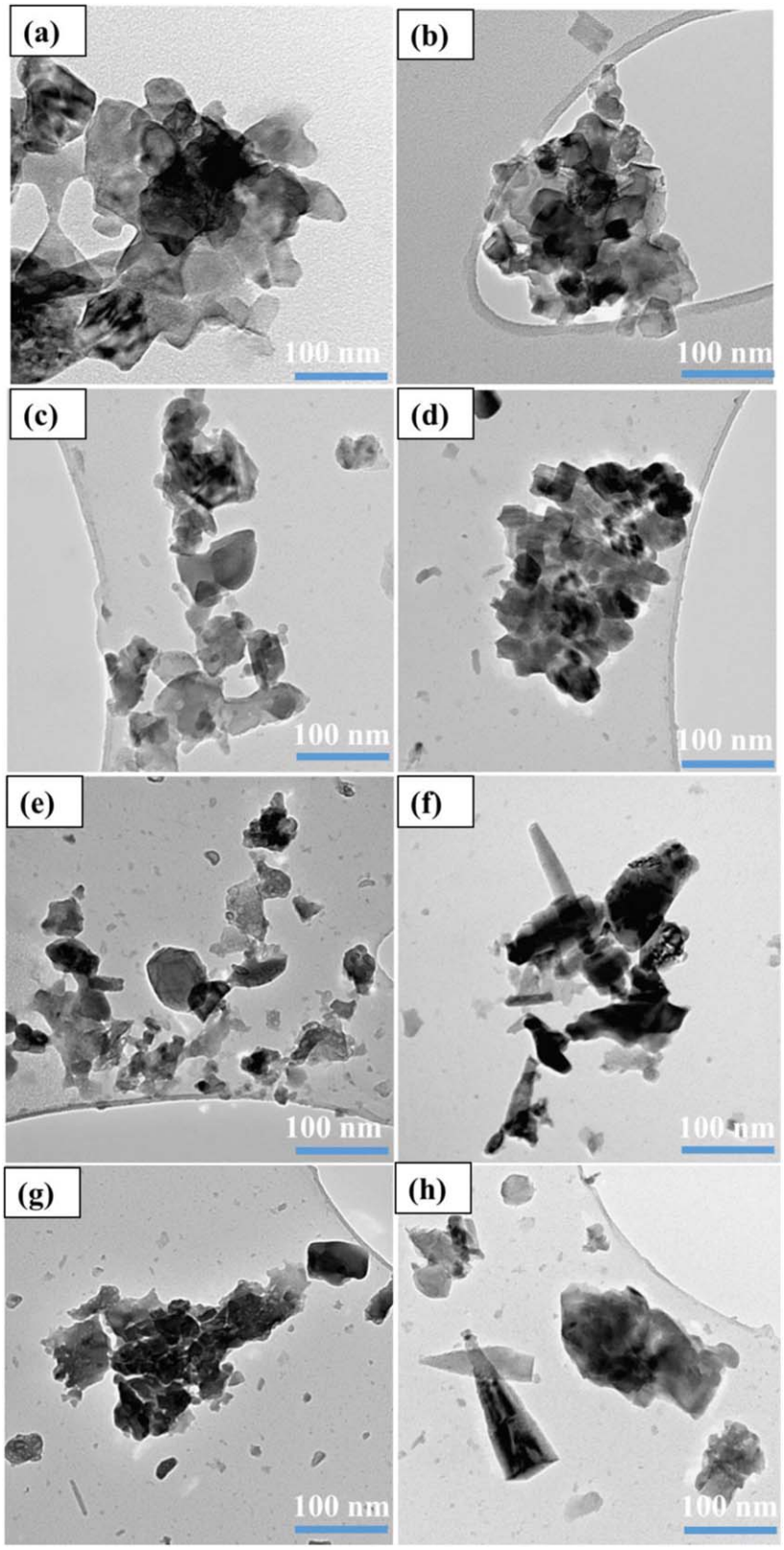

Figure 6. TEM images of the (a) un-doped MMSS, (b) x = 0.2% (c) 0.4% (d) 0.6% (e) 0.8% (f) 1.2% (g) 1.4% and (h) 1.8% Er^{3+}.

attributed to the carbon tape attached to the sample holder during sample preparation for the EDS measurements [29]. Note that the Er was not detected in all of the doped samples and that can possibly be attributed to the low Er^{3+} concentrations, which were not sensitive to the EDS technique used in this study. Figure 4 presents the elemental map of the un-doped MMSS. The individual and layered image shows that Mg, Sr, Al and O elements are distributed all over the surface.

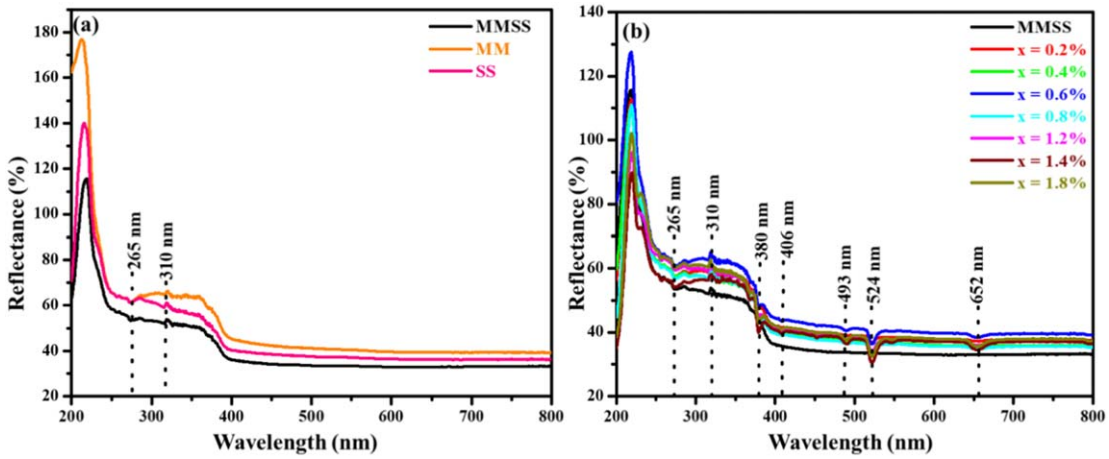

Figure 7. UV-Visible reflectance spectra of the (a) un-doped MMSS, MM, SS phases (b) MMSS and MMSS:x% Er^{3+} ($0 \leqslant x \leqslant 1.8$) series.

3.3. SEM analysis

The morphology of the un-doped and MMSS:x% Er^{3+} ($0 \leqslant x \leqslant 1.8$) samples are shown in figure 5. For the un-doped and lower concentrations $0.2 \leqslant x \leqslant 0.4$ shown in figures 5(a)–(c), the morphology consists of the irregular particles closely packed and distributed over the sample surface. The particles are smaller and highly agglomerated to each other at $x = 0.4$. For the $0.6 \leqslant x \leqslant 0.1.2$ the morphology starts to transform from irregular particles to rods-like structures. The degree of rods-like structures seem to be increasing with Er^{3+} concentration. At the higher Er^{3+} concentrations $1.4 \leqslant x \leqslant 1.8$, the rod-like structures seems to be transforming into the bigger particles of different shapes. Therefore, the results clearly suggest that the surface morphology highly depends on the Er^{3+} doping concentration.

3.4. TEM analysis

The TEM analysis technique was further used to estimate the particle sizes of the prepared nanopowders. The image of the un-doped MMSS is illustrated in figure 6(a). It shows particles that are closely packed together with the estimated particle size around 51 nm. Generally, all other Er^{3+} doped ($0.2 \leqslant x \leqslant 1.8$) samples clearly indicate that the particle sizes are at least below 50 nm. It is interesting to realize that the rods-like structures are clearly observed at $x = 0.6\%$ Er^{3+}, which agrees very well with the SEM results in figure 5(d). From $x \geqslant 0.6\%$, it can be seen that the average particle sizes get bigger as it was also observed on the SEM results shown in figure 5. The results show that varying the Er^{3+} doping concentration influences the average particle sizes and shapes.

3.5. UV-Visible reflectance analysis

Figure 7 display the UV-Visible reflectance spectra of the un-doped MMSS, SS, MM and MMSS:x% Er^{3+} ($0 \leqslant x \leqslant 1.8$) samples. From figure 7(a), it can be seen that the un-doped MMSS, SS and MM samples shows broad absorption bands at around 265 and 310 nm. The absorption band at 265 nm is related to the defect levels of the phases present in the lattice. In particular, absorption band arise from the $O^{2-} \rightarrow Al^{3+}$ charge transition in $MgAl_2O_4$ phase during the excitation of electrons from the valence band to the conduction band [29, 30]. The obseved absoprtion band in all four phases of MMSS at around 310 nm is attributed to the change of lamp to the other lamp during the reflectance measurement on the system [31]. When considering the Er^{3+} doped samples shown in figure 7(b), it can be seen that there are additional five sharp absorption bands located at 380, 406, 493, 524 and 652 nm. These absorption peaks are attributed to f-f transitions in Er^{3+} ions from the ground state $^4I_{15/2} \rightarrow {}^2H_{9/2}$, $^4G_{11/2}$, $^4F_{3/2}$, $^2H_{11/2}$ and $^4F_{9/2}$, respectively [32]. The results clearly shows that the addition of the Er^{3+} concentration to the un-doped sample results in new absorption peaks.

3.6. Photoluminescence analysis

The photoexcitation and photoluminescence (PL) spectra of the mixed phases of the un-doped MMSS, MM, SS and MMSS:x% Er^{3+} ($0 \leqslant x \leqslant 1.8$) series are presented in figure 8. PL analysis of un-doped samples revealed three excitation peaks located around 234 nm, 285 nm and 310 nm when monitoring the emission peak at 653 nm. The observed excitation peaks at 234 nm and 285 nm are certainly attributed to the band-to-band excitation [33] and neutrally charged vacancy known as F center [34], respectively. The 310 nm excitation peak

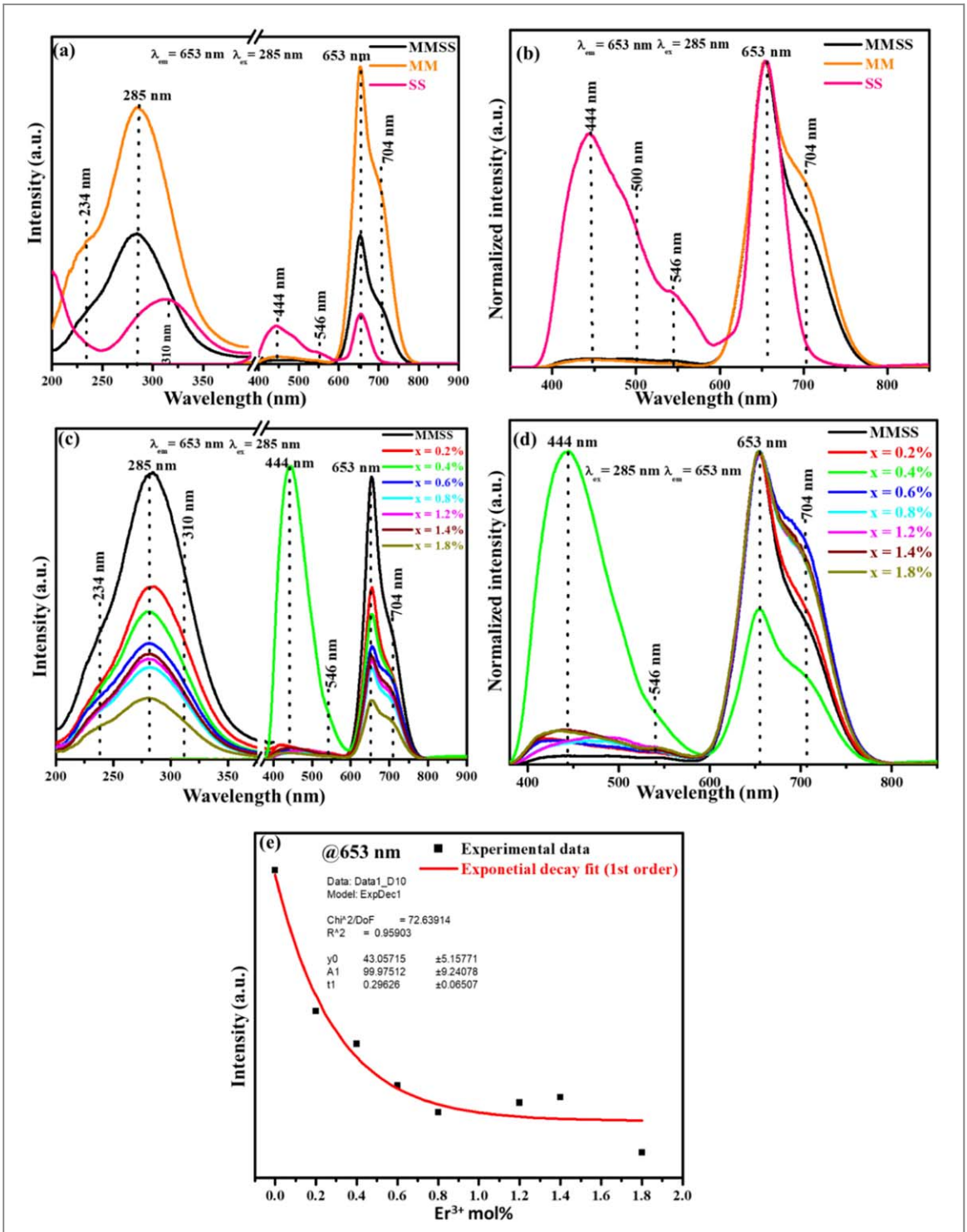

Figure 8. (a) Excitation and emission spectra of the un-doped MMSS, MM, SS (b) normalized emission spectra of the MMSS, MM, SS (c) excitation and emission spectra of the MMSS:x% Er^{3+} ($0 \leqslant x \leqslant 1.8$) series (d) normalized emission intensity and (e) emission intensity as a function of Er^{3+} concentration for the 653 nm emission.

can be attributed to the defect levels within the $SrAl_2O_4$ of the SS phase [35]. There are four emissions peaks located at around 444, 546, 653 and 704 nm when monitoring 285 nm excitation. Peaks at 444 and 546 nm are assigned to the defect levels within the F and F_2—centers in pure *a* -Al_2O_3 for both phases of $SrAl_2O_4$ and $Sr_3Al_2O_6$ phases [36], which are evidently shown by the normalized emission spectra (see figure 8(b)). It can observed from figure 8(b) that there is a shoulder appearing at 500 nm which is attributed to the defect level within the F_2—center of Al_2O_3 of the $SrAl_2O_4$ phase [37]. Previously, Balakrishnan *et al* [8] reported emission peaks at 425, 432 and 495 nm to be from defect band transition and band to band transition for MgO nanoparticles, hence the observed emissions at 444 and 500 nm can also be attributed to the defect level within

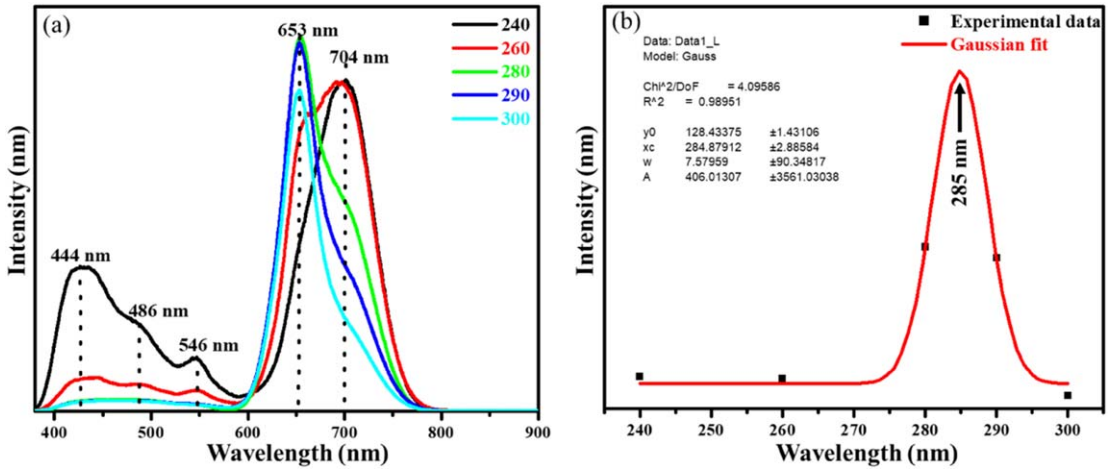

Figure 9. (a) The emission spectra of the un-doped MMSS sample at various excitation wavelength and (b) emission intensity as a function of excitation wavelength.

the MgO phase. Emission peak observed at 653 nm is associated with the abundance of oxygen vacancy within the lattice of all phases maybe due to higher calcination temperature [33]. On the other hand, the green and red emission peaks at 546 and 653 nm, respectively are due to Er^{3+} ions. These peaks are respectively attributed to $^4S_{3/2} \rightarrow {}^4I_{15/2}$ and $^4F_{9/2} \rightarrow {}^4I_{15/2}$ transitions of Er^{3+} [38]. Similar emissions were reported by Wei *et al* [39]. The emission peak at 704 nm is originating from the $MgAl_2O_4$ defects. Taking into account the annealing temperature considered by Yoon *et al* [37] and this study, it is indeed reasonable to conclude that 704 nm for the un-doped sample is originating from the $MgAl_2O_4$. Figure 8(c) shows the excitation and emission spectra of the MMSS:x% Er^{3+}, it can be observed that doping the MMSS did not results in new emission peaks which is evidently shown by the normalized emission spectra in figure 8(d). The same emission peaks observed in figures 8(a) and (b) are also observed in (c) and (d). The emission intensity for the 653 nm peak as a function of Er^{3+} concentration is shown in figure 8(e). For the investigated range, the results revealed an exponetial decrease of emission intensity as Er^{3+} concentration was increased. The decrease in luminescence with an increase in Er^{3+} for the 653 nm peak is attributed to the concentration quenching [40], which is induced by the rates of non-radiative transitions known as the cross-relation or migration between the activator ions being increased [41]. In order to enhance and optimize the 653 nm emission intensity in MMSS:x% Er^{3+} mixed phases, it is recommended that the window 0%–0.4% Er^{3+} concentration be investigated to explore the optimum Er^{3+} concentration into these mixed phases material. However, for the emission peak at 444 nm, the optimum luminescence intensity is found at $x = 0.4\%$ Er^{3+} concentration.

The un-doped MMSS was excited by different wavelengths (240–300 nm) in order to obtain and confirm the optimum excitation wavelength and the results are shown in figure 9(a). The result indicate that there are five emission peaks located at 444, 486, 546, 653 and 704 nm under the excitation of 240 nm. These emissions are attributed to arise from the same notion as discussed above. The shoulder at 486 nm is in this case clearly visible, this emission may be a second order peak from the excitation of 240 nm. Figure 9(b) shows the emission intensity as a function of excitation wavelength and the results revealed the Gaussian behaviour with the maximum at 285 nm, which correspond to the excitation wavelengths used in figure 8.

Figure 10 present the proposed excitation and emission pathway mechanism of the un-doped $MgAl_2O_4$, MgO, $SrAl_2O_4$ and $Sr_3Al_2O_6$. The pathways proposed are based on the PL results displayed in figure 8. Figures 10(a) and (b) shows the mechanism for the $MgAl_2O_4$ and MgO. Considering the band gaps of the $Sr_3Al_2O_6$ (6.3 eV) [9] and $SrAl_2O_4$ (6.5 eV) [10] into account, it can be seen as shown in figures 10(b) and (c) that the 310 nm (4 eV) excitation energy is lower than the energy band gaps of both $Sr_3Al_2O_6$ and $SrAl_2O_4$ phases, indicating that this excitation goes to an intermediate energy level below the conduction band. The excited electrons are de-excited by non-radiative relaxation through different channels resulting in the observed emissions. Figure 10(e) shows the resulted mechanism of Er^{3+} from the 285 nm excitation wavelength which produced the emissions at 546 and 653 nm.

The radiative lifetime measurements of the prepared nanopowders were undertaken at 285 nm excitation and 653 nm emission. Figure 11(a) shows the exponential decay curves of the un-doped MMSS, MM and SS, while the MMSS:x% Er^{3+} ($0 \leqslant x \leqslant 2$) series is shown in figure 11(b). Generally, all of the samples exhibit the same afterglow phosphorescence mechanism and were fitted using the second order exponential decay [32],

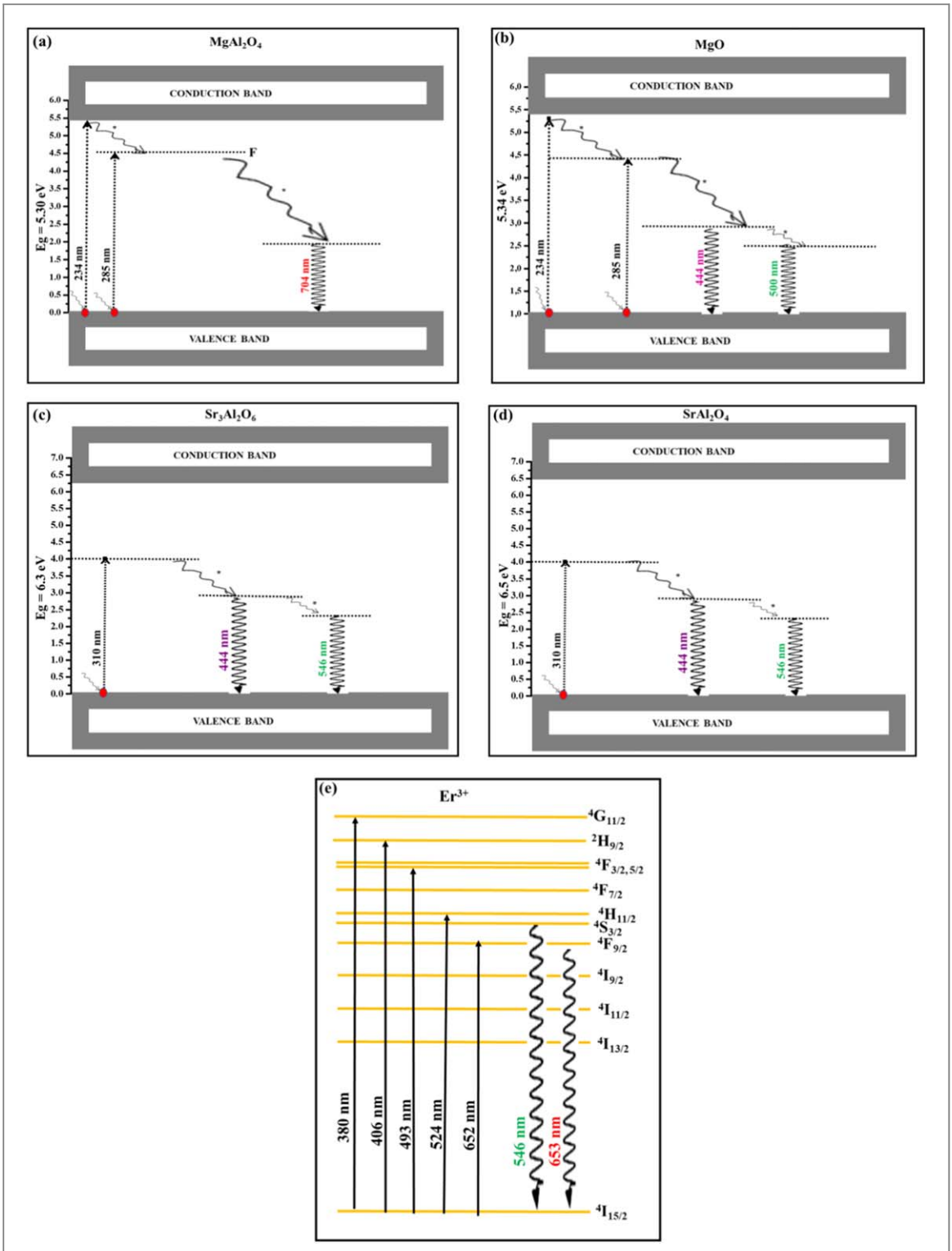

Figure 10. The proposed excitation and emission pathway mechanism of the (a) $MgAl_2O_4$, (b) MgO, (c) $Sr_3Al_2O_6$ (d) $SrAl_2O_4$ and Er^{3+}.

shown in equation (1).

$$I(t) = I_0 + A_1 e^{\left(-\frac{t}{\tau 1}\right)} + A_2 e^{\left(-\frac{t}{\tau 2}\right)} \quad (1)$$

Where $I(t)$ represent the phosphorescent intensity, I_o is the initial luminescence intensity, A_1 and A_2 are constants which contribute to the fast and slow decay component and t is the time of measurement. The τ_1 and τ_2 are the fast and slow decay time values are presented in table 3.

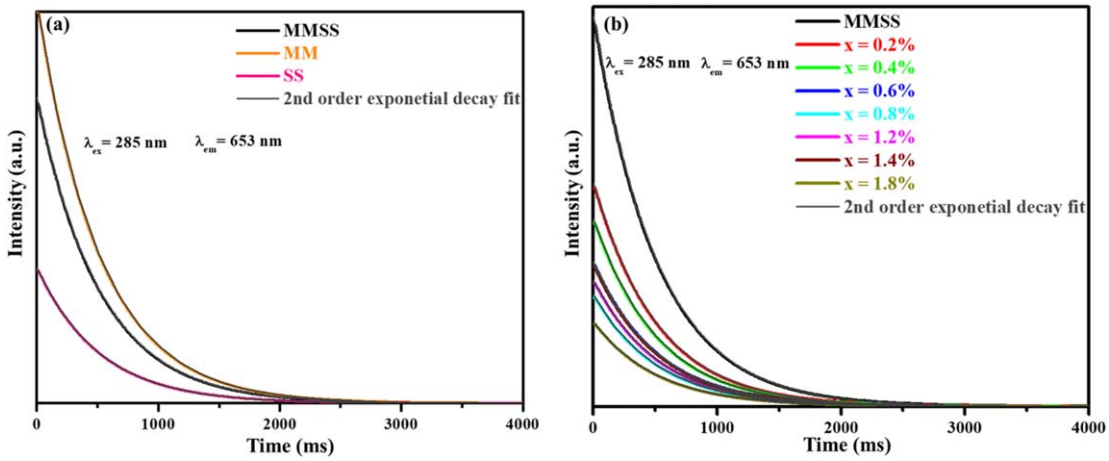

Figure 11. The exponential decay curves of the 653 nm emission for the (a) un-doped MMSS, MM, SS and (b) MMSS:x% Er^{3+} ($0 \leqslant x \leqslant 2$) series.

Table 3. Summary of samples identification and decay times.

	Decay times	
Sample ID	τ_1 (ms)	τ_2 (ms)
MMSS	514.51 ± 0.46	1346.49 ± 465.35
MM	515.93 ± 1.01	1025.63 ± 298.14
SS	514.14 ± 0.26	1912.33 ± 575.85
x = 0.2%	514.12 ± 0.28	1885.80 ± 675.10
x = 0.4%	514.55 ± 0.46	1356.27 ± 470.78
x = 0.6%	514.28 ± 0.25	2050.71 ± 532.80
x = 0.8%	514.05 ± 0.16	4818.29 ± 1267.45
x = 1.2%	514.30 ± 0.23	2363.37 ± 597.76
x = 1.4%	515.01 ± 0.66	1116.79 ± 306.79
x = 1.8%	513.98 ± 0.16	4274.02 ± 995.93

4. Conclusion

The un-doped MMSS, SS, MM and MMSS:x% Er^{3+} ($0 \leqslant x \leqslant 2$) series were successfully prepared by the citrate sol-gel method. The XRD results showed that the structure of the prepared nanopowders consists of the mixture of the cubic ($MgAl_2O_4$, MgO and $Sr_3Al_2O_6$) and monoclinic $SrAl_2O_4$ phases. Varying the Er^{3+} concentration did not affect much the crystal structure of the MMSS phases. Electron microscopy results showed that doping affected the morphology of the prepared powders. The reflectance spectra showed absorption bands at 210, 265, 310, 380, 406, 493, 524 and 652 nm which were attributed to the $MgAl_2O_4$, $Sr_3Al_2O_6$ host and Er^{3+} ions. Vaying the Er^{3+} concentration resulted in addition of absorption peaks. PL results showed four emission peaks located at 444, 500, 546, 653 and 704 nm. These peaks were attributed to the $MgAl_2O_4$, $Sr_3Al_2O_6$ and $SrAl_2O_4$ phases. Increasing the Er^{3+} concentration lead to the 653 nm emission luminescence quenching.

Acknowledgments

This research work is supported by the South African National Research Foundation (NRF) Thuthuka programme (fund number: UID 99266 and 113947), NRF incentive funding for rated researchers (IPRR) (Grant No: 114924). Dr James Wesley-Smith at Electron Microscopy Unit at Sefako Makgatho Health Science University is acknowledged for the SEM and TEM imaging.

ORCID iDs

S V Motloung https://orcid.org/0000-0002-4085-3927

References

[1] Mhlongo M R, Koao L F, Kroon R E, Motaung T E and Motloung S V 2019 *J. Mol. Struct.* **1184** 92–101
[2] Nassar Y M Y, Ahmed S I and Samir I 2014 *Mol. Bio. Spectro.* **131** 329–34
[3] Zhang J, Zhang X, Shi J and Gong M 2011 *J. Lmin.* **131** 2463–7
[4] Calderon-Olvera R M, Albanes-Ojeda E A, Garcia-Hipolito M, Hernandez-Alcantara J M, Alvarez-Perez M A, Falcony C and Alvarez-Fregoso O 2018 *Ceram. Inter.* **44** 7917–25
[5] Melato L T, Motaung T E, Ntwaeaborwa O M and Motloung S V 2017 *Opt. Mat.* **66** 319–26
[6] Motloung S V, Dejene B F, Kroon R E, Ntwaeborwa O M, Swart H C and Motaung T E 2017 *Optik* **131** 705–12
[7] Raghavendra M, Lalithamba H S, Sharath B S and Rajanaika H 2017 *Scien. Ira.* **24** 3002–13 (https://www.researchgate.net/deref/http%3A%2F%2Fdx.doi.org%2F10.24200%2Fsci.2017.4491)
[8] Balakrishman G, Velavan R, Batoo K M and Raslan E H 2020 *Res. Phy* **16** 103013
[9] Akiyama M, Xu C N, Liu Y, Nonaka K and Watanabe T 2002 *J. Lumin.* **97** 13–5
[10] Mindru I, Gingasu D, Patron L, Marinescu G, Culita D C, Calderon-Moreno J M, Preda S and Secu M 2017 *Ceram. Inter.* **43** 16668–75
[11] Misevicius M, Jorgenses J and Kareiva A 2013 *Mat Sci.* **19** 38–42
[12] Sharma S K 2014 *Strontium Aluminates-from Synthesis to Applications* (Lampert Academic Publishing) (https://www.morebooks.shop/store/gb/book/strontium-aluminate-phosphors-from-synthesis-to-applications/isbn/978-3-659-29605-5)
[13] Garcia C K, Diaz-Torres L A, Sala P, Guzman M and Angeles-chavez C 2015 *Mat. Sci. Sem. Pro.* **37** 105–11
[14] Amini M M, Mirzaee M and Sepanj N 2007 *Mater. Res. Bull.* **42** 563–70
[15] Kashii N, Maekawa H and Hinatsu Y 1999 *J. Am. Ceram. Soc.* **82** 1844–8
[16] Alvar E N, Rezaei M and Alvar H N 2010 *Powder Technol.* **198** 275–8
[17] Zhai B, Ma Q, Xiong R, Li X and Huanga Y M 2016 *Mater, Res. Bull.* **75** 1–6
[18] Rezgui S and Gates B C 1997 *J. Non-Cryst. Solids.* **210** 287–97
[19] Maphiri V M, Wesley-Smith J and Motloung S V 2019 *J. Lum.* **215** 116710
[20] Verma S, Mishra A, Bhuie M and Singh N K 2018 *Int. J. Res. Elect. Com.* **6** 2348–2281 (http://nebula.wsimg.com/22111750e32c36c1a24657d14e9aac16?AccessKeyId=DFB1BA3CED7E7997D5B1&disposition=0&alloworigin=1)
[21] Mironova-Ulmane N, Sarakovskis A and Skvortsova V 2015 *Phy. Pro.* **76** 106–10
[22] Choudhary A K, Dwivedi A, Bahadur A and Rai S B 2017 *Spe. Acta. Mol. Bio. Spec.* **185** 155–62
[23] Singh V, Seshadri M, Singh N and Mohapatra M 2019 *J. Mater. Sci. Elec.* **30** 2927–34
[24] Wu S Y, Dong H N, Wei W and Naturforch Z 2004 *Zeitschrift für Naturforschung A* **59** 341–5
[25] Dlamini C, Mhlongo M R, Koao L F, Motaung T E, Hlatshwayo T T and Motloung S V 2020 *Appl. Phys.* A **126** 75
[26] Ayvacikli M, Kotan Z, Ekdal E, Karabulut Y, Canimoglu A, Garcia and Guinea J 2013 *J. Lumin* **144** 128–32
[27] Hou Q, Meng F and Sun J 2013 *Nano Res. Lett.* **8** 144
[28] Cullity B D and Sock S R 2001 *Elements of X-ray Diffraction* 3rd edn (Reading: Pearson Education) pp 402–4 (https://www.pearson.com/store/p/elements-of-x-ray-diffraction/P100000151708/9780201610918)
[29] Koao L F, Dejene B F, Hone F G, Swart H C, Motloung S V, Motaung T E and Pawade V B 2018 *J. Limin.* **200** 205–15
[30] Mostafa Y, Nassar S I and Ahmed S A 2014 *Mol. Bio. Spectro.* **334** 329–34 (https://www.researchgate.net/deref/http%3A%2F%2Fdx.doi.org%2F10.1016%2Fj.saa.2014.04.040)
[31] Motloung S V, Tshabalala K G, Kroon R E, Hlatshwayo T E, Mlambo M and Mpelane S 2019 *J. Mol. Struct.* **1175** 241–52
[32] Singh B P, Parchur A K, Singh R K, Ansari A A, Singh P and Rai S B 2013 *Phy. Chem. Phys.* **15** 3480
[33] Tabaza W A I, Swart H C and Kroon R E 2014 *J. Lumin.* **148** 192–7
[34] Maphiri V M, Dejene F B and Motloung S V 2017 *Res. Phy.* **7** 3510–21
[35] Melato L T, Motaung T E, Ntwaeborwa O M and Motloung S V 2017 *Opt. Mat.* **66** 319–26
[36] Tamrakar R K and Upadhyay K 2017 *Res. J. Recent Sci.* **6** 28–31 (http://www.isca.in/rjrs/archive/v6/i4/5.ISCA-RJRS-2017-038.php)
[37] Mikenda W and Presinger A 1981 *J. Lumin.* **26** 53–83
[38] Taherunnisa S K, Krishna D V, Reddy K, SambasivaRao T, Rudramamba K S, Zhydachevskyy Y A, Suchocki A, Piasecki and Reddy M R 2019 *Opt. Matt* X **3** 100034
[39] Wei L, Xinzheng L, Lu H, Huiqing L, Yingjuan C, Pingguang D and Xiaowei L 2015 *Inte. Jour. Photo* **8** 376202
[40] Motloung S V, Dejene F B, Kroon R E, Swart H C and Ntwaeaborwa O M 2015 *Phys.* B **468–469** 11–20
[41] Grube J, Sarakovskis A, Doke G and Springis M 2014 *Lat. Journ. Phys. Tech. Scie.* N **3** 0018